JℲM PAPERS

Wall shear stress from jetting cavitation bubbles: influence of the stand-off distance and liquid viscosity

Qingyun Zeng[1], Hongjie An[2],† and Claus-Dieter Ohl[3],†

[1]Division of Physics and Applied Physics, School of Physical and Mathematical Sciences, Nanyang Technological University, 21 Nanyang Link, Republic of Singapore 637371

[2]Queensland Micro and Nanotechnology Centre, Griffith University, Nathan, QLD 4111, Australia

[3]Department Soft Matter, Institute for Physics, Otto-von-Guericke-University Magdeburg, Universitätsplatz 2, 39016 Magdeburg, Germany

We study systematically the cavitation-induced wall shear stress on rigid boundaries as a function of liquid viscosity μ and stand-off distance γ using axisymmetric volume of fluid (VoF) simulations. Here, $\gamma = d/R_{max}$ is defined with the initial distance of bubble centre from the wall d and the bubble equivalent radius at its maximum expansion R_{max}. The simulations predict accurately the overall bubble dynamics and the time-dependent liquid film thickness between the bubble and the wall prior to the collapse. The spatial and temporal wall shear stress is discussed in detail as a function of γ and the inverse Reynolds number $1/Re$. The amplitude of the wall shear stress is investigated over a large parameter space of viscosity and stand-off distance. The inward stress is caused by the shrinking bubble and its maximum value τ_{mn} follows $\tau_{mn}Re^{0.35} = -70\gamma + 110$ (kPa) for $0.5 < \gamma < 1.4$. The expanding bubble and jet spreading on the boundary produce an outward-directed stress. The maximum outward stress is generated shortly after impact of the jet during the early spreading. We find two scaling laws for the maximum outward stress τ_{mp} with $\tau_{mp} \sim \mu^{0.2}h_{jet}^{-0.3}U_{jet}^{1.5}$ for $0.5 \leq \gamma \leq 1.1$ and $\tau_{mp} \sim \mu^{-0.25}h_{jet}^{-1.5}U_{jet}^{1.5}$ for $\gamma \geq 1.1$, where U_{jet} is the jet impact velocity and h_{jet} is the distance between lower bubble interface and wall prior to impact.

Key words: bubble dynamics, cavitation

† Email addresses for correspondence: hongjie.an@griffith.edu.au, claus-dieter.ohl@ovgu.de

1. Introduction

A bubble collapsing near a rigid boundary develops a fast and directed flow towards the wall. In addition to the normal stress arising from the stagnation pressure, very high wall tangential stresses are created at some distance from the impact region. These cavitation-induced wall shear stresses are, for example, used for surface cleaning (Ohl *et al.* 2006*a*; Reuter *et al.* 2017) and in biological application (Ohl *et al.* 2006*b*; Rau *et al.* 2006). So far, the direct measurement of the wall shear stresses remains a challenging problem owing to the required high resolution in space and time as a result of the extraordinary fast bubble dynamics. Only a couple of papers report experimental measurements of the wall shear stress, one where a hot-film anemometer was used by Dijkink & Ohl (2008) and a second where an electrochemical method was developed by Reuter & Mettin (2018). Both approaches are limited as they measure at a single point and are affected by their inherent low bandwidth. Interestingly, both techniques report peak values of the wall shear stress of a few kilopascals.

Recent simulations with a sufficiently fine grid reveal the complex boundary flow and wall shear stress distribution from a single cavitation bubble with a wall distance $\gamma = d/R_{max} \approx 1.0$ (Zeng *et al.* 2018*a*), where d is the distance of bubble nucleation and R_{max} the maximum bubble radius. While the overall shape and features of the measurements are similar to the simulations, the peak values in the simulations are 1 to 2 orders of magnitude higher. Although there is no concluding understanding to the cause of such a big discrepancy, it may be the result of the limited bandwidth, spatial resolution and the intrusiveness of the sensor to the flow. The clear advantage of the simulations is the capability to map the spatio-temporal stress pattern acting on the boundary. We find that prior to the impact and spreading of the jet, the inward stress from the shrinking bubble results in peak stress values of a few kPa. In contrast, the stress created by the spreading jet may reach up to 100 kPa and is the result of the fast jet accelerating liquid in the thin gap formed between the lower bubble wall and the boundary.

Over the last decades, the shape and jet velocity of bubbles have been studied in detail, particularly as a function of the stand-off distance (Philipp & Lauterborn 1998; Supponen *et al.* 2016). In contrast, the flow bounded by the lower bubble surface and the rigid boundary has received much less attention. Reuter & Kaiser (2019) demonstrated that even for very small stand-off distances, a thin yet finite liquid film separates the bubble from the rigid boundary. They measured systematically the liquid film thickness $h(t)$ for a range of stand-off distances γ by combining shadowmetry with a total internal reflection method and provided an empirical correlation $h \sim \gamma^{4.86}$ for γ between 0.47 and 1.07 for the minimum thickness. On the simulation side, Lechner *et al.* (2020) successfully compared these measurements with numerically obtained gap thickness with a VoF method based solver of the flow. From the empirical relation, it is evident that the liquid film thickness decreases with γ and also the speed of the jet at impact decreases (Philipp & Lauterborn 1998; Supponen *et al.* 2016). Thus one may expect an optimum stand-off distance where both competing factors provide a maximum or optimum shear stress for applications, i.e. following the argument in surface cleaning experiments of Reuter & Mettin (2016).

In addition to the stand-off distance, the shear viscosity of the liquid affects the wall shear stress through two routes. First, just by definition for a Newtonian fluid, the wall shear stress is defined as the product of the wall shear rate and the dynamic viscosity μ. The viscosity also affects the overall flow field and, in particular, the boundary layer thickness (Schlichting & Gersten 2016), the jet shape and its speed non-trivially and as a function of γ (Popinet & Zaleski 2002).

Simulation has been broadly used to resolve the rapid and microscopic scales dynamics from jetting bubbles near rigid boundaries since the pioneering work of Plesset & Chapman (1971). Many studies use the efficient boundary element method (BEM) (Blake & Gibson 1987) to solve the complex bubble deformation with various implements. To name a few, Lee, Klaseboer & Khoo (2007) and Wang (2014) applied artificial energy loss models to achieve multiple rebounding of the bubble; Zhang & Liu (2015) improved the BEM with topology optimization and applied the technique to study the flow fields and bubble splitting during bubble collapsing near a rigid boundary (Zhang, Li & Cui 2015; Li *et al.* 2016); Chahine *et al.* (2016) coupled the BEM with fluid–structure interaction to model the particle motion arising from a jetting bubble near a solid boundary. Limited to the potential flow model, liquid viscosity is not modelled in BEM. In contrast, numerical methods based on solving the Euler equations are able to capture sharp interface and shock-wave with high-order schemes (Johnsen & Colonius 2009; Lauer *et al.* 2012; Beig, Aboulhasanzadeh & Johnsen 2018; Trummler *et al.* 2020). Recently, the VoF method based on solving the compressible Navier–Stokes (NS) equations is attracting increased attention owing to its compatible implementations of the compressibility, viscosity, surface tension, complex bubble deformation and even complex boundaries (Han *et al.* 2015; Koch *et al.* 2016; Denner, Evrard & van Wachem 2020; Zeng, Gonzalez-Avila & Ohl 2020).

To gain more knowledge, we expand our previous numerical simulations to a parameter study by varying the liquid viscosity and the stand-off distance to identify, for example, modalities of highest wall shear stress. To do so, we first validate our model against relevant experiments by comparing them to the simulated bubble shape and the time-dependent film thickness. Then a detailed description on the influence of liquid viscosity and stand-off distance will be given. We discuss separately the maximum wall stresses from the inward and outward flow as a function of the inverse Reynolds number, $1/Re$, and the stand-off distance γ. The results are summarized through scaling laws for the maximum wall shear stress.

2. Methodology

In this paper, we use the well-validated VoF solver (Zeng *et al.* 2018*a*,*b*, 2020; Gonzalez-Avila *et al.* 2020) to conduct a study of the wall shear stress generated from expanding and collapsing cavitation bubbles as a function of viscosity and initial distance to a solid boundary. The problem consists of two phases (gas and liquid), where both are compressible and immiscible Newtonian fluids. As heat and mass transfer between two phases are negligible (Koukouvinis *et al.* 2018; Zeng *et al.* 2020), the governing equations for the flow are the equations of continuity and momentum:

$$\frac{\partial \rho}{\partial t} + \nabla \cdot (\rho \boldsymbol{u}) = 0, \tag{2.1}$$

$$\frac{\partial \rho \boldsymbol{u}}{\partial t} + \nabla \cdot (\rho \boldsymbol{u}\boldsymbol{u}) = -\nabla p + \nabla \cdot \boldsymbol{s} + \boldsymbol{f_\delta}, \tag{2.2}$$

where ρ, $\boldsymbol{u}$, t and p are the density, velocity, time and pressure, respectively. The role of viscosity is included as the viscous stress tensor $\boldsymbol{s} = \mu[\nabla \boldsymbol{u} + \nabla \boldsymbol{u}^T - \frac{2}{3}(\nabla \cdot \boldsymbol{u})\boldsymbol{I}]$, with the dynamic viscosity μ and an identity tensor $\boldsymbol{I}$. Here, $\boldsymbol{f_\delta}$ is the surface tension term modelled with the so-called continuous surface force (CSF) method (Brackbill, Kothe & Zemach 1992).

The cavitation bubble content is numerically treated as a non-condensable gas, which follows a polytropic equation of state (EOS):

$$\frac{p}{\rho^\kappa} = \frac{p_n}{\rho_n^\kappa}, \qquad (2.3)$$

where $p_n = 101325$ Pa and $\rho_n = 1.2$ kg m^{-3} are the reference pressure and density of the gas, $\kappa = 1.4$ is the specific heat ratio or adiabatic exponent of the gas phase and the surrounding liquid is modelled as a Tait-compressible liquid:

$$\rho = \rho_0 \left(\frac{p + B}{p_0 + B} \right)^{1/\Gamma}, \qquad (2.4)$$

where $p_0 = 101325$ Pa and $\rho_0 = 1000$ kg m^{-3} are the reference density and reference pressure, respectively. Here, $\Gamma = 7.15$ is the Tait exponent and $B = 3046$ bar is the Tait pressure. To capture the bubble interface, a transport equation for the volume fraction of the liquid phase α is solved (Miller *et al.* 2013; Koch *et al.* 2016; Zeng *et al.* 2018*b*):

$$\frac{\partial \alpha}{\partial t} + \nabla \cdot (\alpha \boldsymbol{u}) + \nabla \cdot (\alpha(1 - \alpha)\boldsymbol{U_r}) = \alpha(1 - \alpha) \left(\frac{\psi_g}{\rho_g} - \frac{\psi_l}{\rho_l} \right) \frac{\mathrm{D}p}{\mathrm{D}t} + \alpha \nabla \cdot \boldsymbol{u}, \qquad (2.5)$$

where $\psi = \mathrm{D}\rho/\mathrm{D}p$ is the compressibility computed based on the EOS. The subscripts l and g represent the liquid and the gas phases, respectively, and $\boldsymbol{U_r}$ is the relative velocity between two phases and acts as an artificial compressible term ensuring a sharp interface (Rusche 2003).

Simulations were performed using OpenFOAM (Weller *et al.* 1998), where the compressible Navier–Stokes (NS) equations are discretized and solved with the VoF method to obtain the velocity and pressure field and the time-dependent bubble interface. The EOS was used to compute the compressibility and density of each phase based on the pressure. When solving the equations, the time step is adaptively updated by specifying the Courant number as 0.1 to ensure the stability of the solution. Details of the numerical method are documented in Zeng *et al.* (2018*a*,*b*, 2020).

The bubbles studied here have a maximum equivalent radius $R_{max} \approx 400$ μm similar to those in Reuter & Kaiser (2019). To simplify the simulation and limit the effects from distant boundaries, we choose an axisymmetric domain of 10 mm $\times$ 10 mm. The mesh is refined successively so that it has a finer spacing of $\Delta x = 1.5$ μm closer to the bubble but coarsens quickly further away. This non-uniform mesh allows us to conduct high-resolution simulations with moderate computational resources. The initial bubble is nucleated as a high-pressure gas sphere with its centre located at a distance of d from the wall, therefore at a non-dimensional stand-off distance $\gamma = d/R_{max}$. The rigid wall below the bubble is modelled as a no-slip boundary. The near-boundary mesh is gradually refined even further down to a spacing of $\Delta x = 50$ nm to make sure that the boundary layer flow for the expected high values of the strain rates is resolved adequately. Outer boundaries are considered far fields. Vanishing gradient of velocities are applied at outer boundaries to allow in and out flux. For pressure field, the vertical and radial outer boundaries are set as the ambient pressure $P_\infty = 101325$ Pa and a non-reflecting boundary, respectively. The gas bubble is initialized with a radius $R(t = 0) = 25$ μm and a high pressure P_0. The high pressure P_0 is adjusted to meet the experimental period of growth and collapse of each bubble in § 3 but is kept constant as $P_0 = 2700$ bar for the remaining sections.
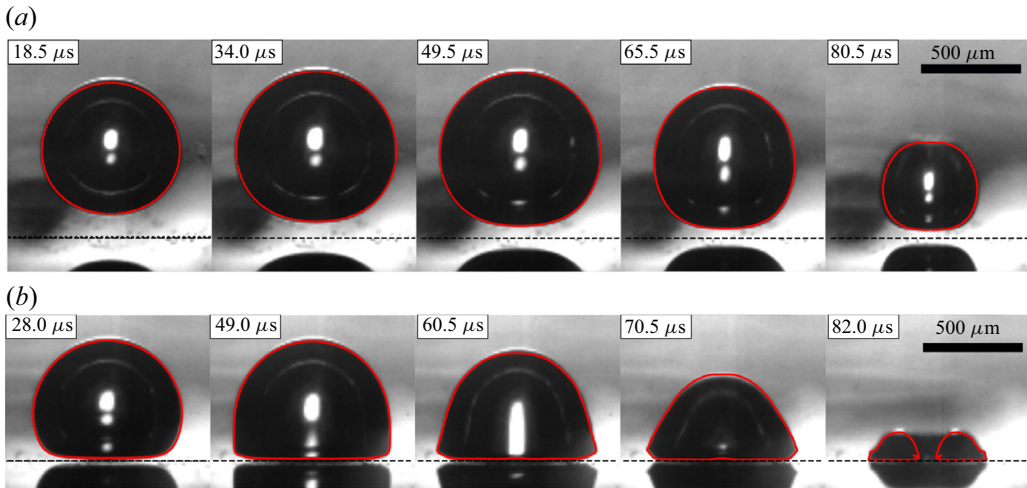
(*a*)

(*b*)

Figure 1. Comparison of the computed bubble dynamics and experimental results from Reuter & Kaiser (2019). Red contours represent the computed bubble interface. Dashed lines indicate the positions of the solid boundaries. (*a*) Experiment $-\gamma = 1.05$, $R_{max} \approx 420$ μm; simulation $-\gamma = 1.05$, $R_{max} = 410$ μm, $P_0 = 2900$ bar. (*b*) Experiment $-\gamma = 0.56$, $R_{max} \approx 390$ μm; simulation $-\gamma = 0.57$, $R_{max} = 380$ μm, $P_0 = 2300$ bar.

3. Fluid flow near the wall

The model is first tested against bubbles collapsing for $\gamma \leq 1.1$ near a rigid boundary. Reuter & Kaiser (2019) not only measured the bubble shape but also the thickness of the liquid film separating the bubble from the rigid boundary. Two of their high-speed recordings are shown in figure 1 for $\gamma = 1.05$ and $\gamma = 0.56$. The red contours are the bubble interface superimposed on the experimental recording that are taken from the simulations at the same time instance. In figure 1(*a*) for $\gamma = 1.05$, the bubble expands to a nearly spherical shape then shrinks into an elongated bubble with the larger axis oriented normal to the boundary. In the second comparison, figure 1(*b*) checks the simulation against a bubble nucleated closer to the solid boundary with $\gamma = 0.56$. During the expansion, the bubble flattens considerably its lower surface and takes the shape of nearly a hemispherical bubble that changes into a cone-shaped outline before collapsing as a toroidal bubble.

While the agreement with the overall shape of the bubble is a good indicator for the quality of the simulation, the liquid flow very close to the boundary is crucial for obtaining good estimates of the wall shear stress. We therefore compare the thickness of the thin liquid film that separates the bubble from the rigid boundary. Figure 2(*a*) plots the minimum time-dependent thickness, $h(t)$, of the thin film for four pairs of very similar stand-off distances. The lines decorated with dots are the experimental data from Reuter & Kaiser (2019) while solid lines are from simulations. During the early expansion, $h(t)$ drops rapidly for all cases. The decrease slows down in the late expansion. In the later dynamics, $h(t)$ approaches a constant value during collapse for $\gamma \leq 1$, but it increases at the late collapse for $\gamma = 1.2$. These two distinct dynamics result in two different functions of the film thickness at jet impact (see below and figure 2*b*). Please note that in the measurement of Reuter & Kaiser (2019), a flat mirror-like bubble interface is assumed while this is only approximately true. Therefore the measurement overestimates $h(t)$ when the lower bubble interface is curved, which for small stand-off distances is the case only
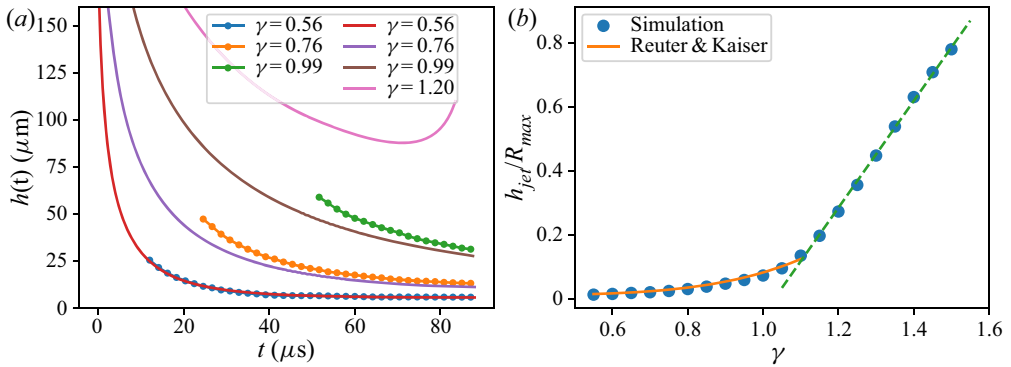
Figure 2. Liquid film dynamics. (*a*) The evolution of the gap thickness for different γ values, lines represent the simulation data while lines with dots are the measurement from Reuter & Kaiser (2019); the experimental and simulation data end at the time of jet impact. In the experiment, $R_{max} = 411$, 419 and 406 μm, for $\gamma = 0.56$, 0.76 and 0.99, respectively; in the simulation, $R_{max} = 409$, 417, 405 and 397 μm for $\gamma = 0.56$, 0.76, 0.99 and 1.2, respectively. (*b*) The gap thickness at jet impact onto the bubble's lower interface, solid line is the fit provided by Reuter & Kaiser (2019) ($\gamma = 0.47$–1.07) and the slope of the green dashed line is 1.

during the early stage of the bubble expansion. For larger stand-off distances, the film is considerably curved (see figure 1*a*).

Next we have a look at the film thickness at the moment the jet contacts the bubble's lower interface, h_{jet}. This is the time just prior to the jet impact when high normal and shortly afterward tangential stresses are experienced by the boundary. Figure 2(*b*) compares the measured film thickness h_{jet} normalized by the maximum bubble radius R_{max} with the simulations (dots). The solid line up to $\gamma = 1.1$ are the empirical correlation found by Reuter & Kaiser (2019), which is $h = 29.2\gamma^{4.86} + 4.74$ (μm) for bubbles with $0.47 < \gamma < 1.07$. This fit is based on 91 experiments with bubble sizes in the interval $385\ \mu$m $< R_{max} < 435\ \mu$m with a mean size of $410\ \mu$m. The simulations are spot on with this empirical fit. Continuing the simulations to larger γ values, we find an approximately linear increase of the height as indicated with the dashed line in figure 2(*b*).

4. Viscous bubble dynamics

Previously, a detailed study of the bubble dynamics and the resulting distribution of the wall shear stress was done for a few selected cases in water at a distance of $\gamma \approx 1$ (Zeng *et al.* 2018*a*). The choice of γ value was motivated for a comparison with an experiment. In the present work, we expand the study to reveal the effect of liquid viscosity μ (from 10^{-3} Pa $\cdot$ s to 0.1 Pa $\cdot$ s) and stand-off distance γ (from $\gamma = 0.5$ to 1.6). The choice of the parameter space is to cover the important transitions (see below sections) while practical for bubble nucleation. For all simulations present below, the initial pressure within the bubble is fixed to 2700 bar, i.e. the initial energy is the same for all simulations. Owing to viscous dissipation, the resulting maximum equivalent radius R_{max} increases slightly from $370\ \mu$m to $400\ \mu$m with decreasing viscosity.

Now we look at how the liquid viscosity influences the bubble dynamics. Here we define the Reynolds number $Re = \rho U_0 R_{max}/\mu$, where $U_0 = \sqrt{P_\infty/\rho}$ is a referenced velocity from the ambient pressure P_∞ and R_{max} the maximum bubble radius of each simulation. The dimensionless numbers chosen here are related to the shrinkage instead of the growth of the bubble, similar to Jayaprakash, Hsiao & Chahine (2012).
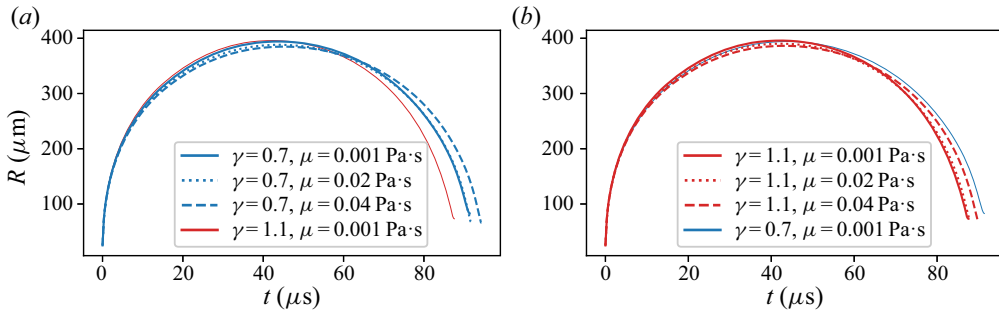
Figure 3. Comparison of bubble's equivalent radius for different viscosities: (*a*) $\gamma = 0.7$; (*b*) $\gamma = 1.1$. The bubble dynamics for $\mu = 10^{-3}$ Pa · s is drawn in both plots for comparison. The R_{max} is 394 μm, 388 μm, 385 μm in panel (*a*), and 396 μm, 390 μm, 386 μm in panel (*b*) for viscosity 0.001, 0.02, 0.04 Pa · s, respectively.
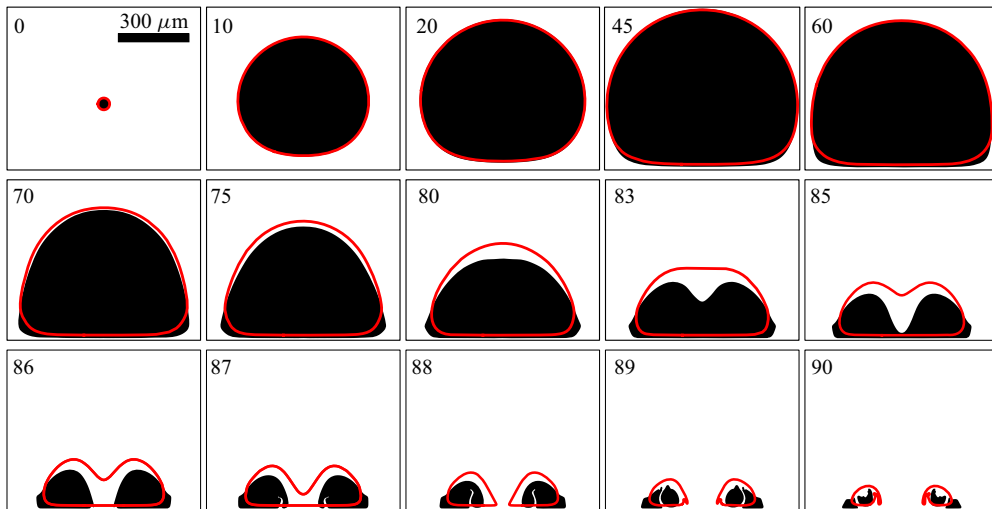
Figure 4. Comparison of the computed bubble shapes for $\gamma = 0.7$ between $\mu = 10^{-3}$ Pa · s (black shapes) and $\mu = 0.02$ Pa · s (red lines). Times are in μs. The lower borderline of each frame represents the solid boundary. The maximum bubble radius R_{max} reduces from 394 μm to 388 μm with increasing viscosity.

In figure 3, we show the comparison of the bubble's equivalent radius for three different viscosities for two selected stand-off distances $\gamma = 0.7$ and $\gamma = 1.1$. It is seen at both γ values that the bubble dynamics is slowed down and R_{max} reduces with increasing viscosity, which is the result of the increasing viscous drag and dissipation (Brennen 2014). Although the evolution of the bubble radius changes only mildly with an increase of liquid viscosity, i.e. from $\mu = 10^{-3}$ Pa · s to $\mu = 0.02$ Pa · s, we find a significant difference in the bubble shape, as shown in figures 4 and 5.

Figure 4 plots the bubble shapes from expansion to collapse for the same stand-off distance $\gamma = 0.7$ but two different viscosities ($\mu = 10^{-3}$ Pa · s, black shape; $\mu = 0.02$ Pa · s, red contour). Bubbles in both liquids acquire an hemispherical shape and collapse into a conical and toroidal shape sequentially, but a clear difference is visible during this dynamics. First of all, the motion of the top interface moving towards the wall is slowed in the more viscous liquid owing to higher viscous drag, which leads to a lower
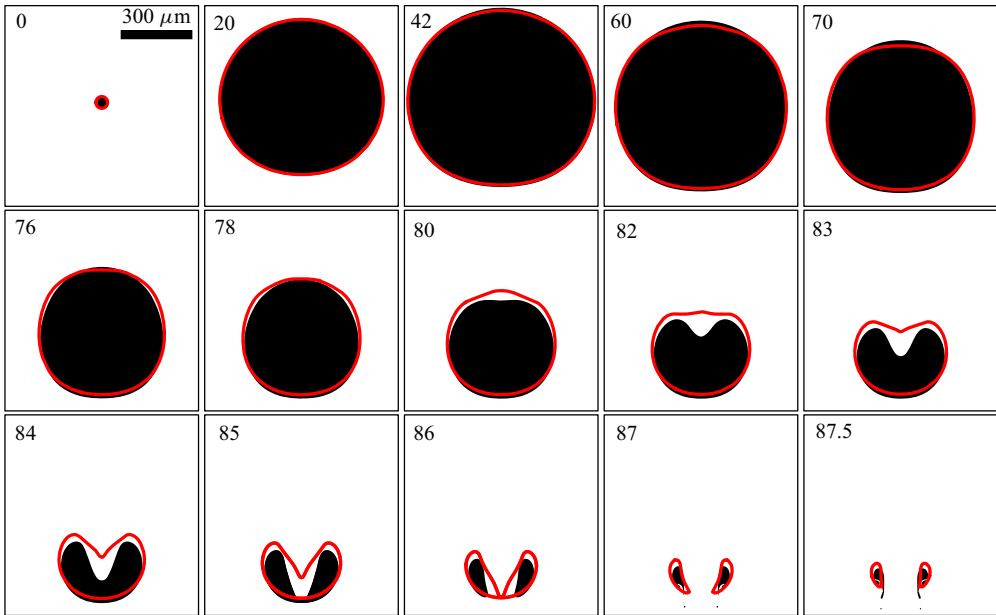
Figure 5. Comparison of the computed bubble shapes for $\gamma = 1.1$ between $\mu = 10^{-3}$ Pa · s (black shapes) and $\mu = 0.02$ Pa · s (red lines). Times are in μs. The lower borderline of each frame represents the solid boundary. The maximum bubble radius R_{max} reduces from 396 μm to 390 μm with increasing viscosity.

jet impact velocity. The dynamics in the near-wall region is greatly affected by the liquid viscosity too, which is attributed to the thicker boundary layer formed in the more viscous liquid. It is seen that the liquid film thickness h_{jet} increases from 8 μm to 20 μm when the liquid viscosity changes from $\mu = 10^{-3}$ Pa · s to $\mu = 0.02$ Pa · s. Additionally, the bubble edge becomes smoother and is lifted further from the wall vertically but closer to the axis horizontally.

A second comparison of the bubble shapes is plotted in figure 5 for a higher stand-off distance $\gamma = 1.1$. Here, we also observe a slower bubble motion and an increase of the liquid film thickness h_{jet} from 53 μm to 75 μm when the liquid viscosity changes from $\mu = 10^{-3}$ Pa · s to a 20 times more viscous liquid $\mu = 0.02$ Pa · s. Interestingly, owing to the stronger viscous drag, the bubble becomes spherical instead of elongated in the more viscous liquid during the early collapse ($42 < t < 80$ μs). Yet at a later time but before the jet formation ($t = 80$ μs), the bubble interface at the axis collapses slower than the nearby interface and the top interface acquires a particular curvature. This arises from a combined effect of viscous drag and the flow induced by the shrinking bubble. Such a curvature may result into a higher jet velocity although occurring in a more viscous liquid, see figure 6(*b*).

Figure 6 depicts the influence of viscosity on four important features of the bubble dynamics for the two selected stand-off distances $\gamma = 0.7$ and $\gamma = 1.1$. In figure 6(*a*), the film thickness is found to increase with viscosity for both γ values and becomes constant in the high $1/Re$ regime for $\gamma = 1.1$. Figure 6(*b*) reveals that the jet velocity, in general, decreases with viscosity and increases with γ. Interestingly, we found one special case ($\gamma = 1.1$ the second marker) where the jet velocity could increase in a more viscous liquid, whose mechanism is related to the particular curved top interface motioned above. The structures of the jet are plotted in figure 6(*c,d*) with the inset depicting the geometry.
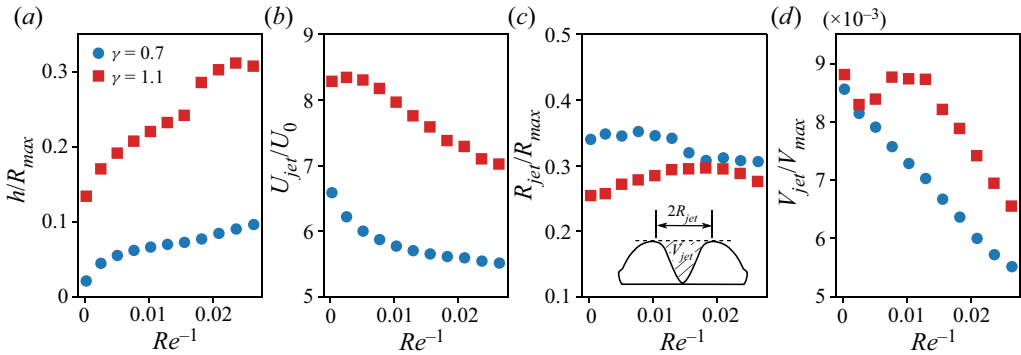
Figure 6. Influence of $1/Re$ number on four important features of the bubble dynamics for two selected stand-off distances $\gamma = 0.7, 1.1$. (*a*) Film thickness, (*b*) jet velocity, (*c*) width of the jet and (*d*) volume of the jet, where V_{max} is the bubble volume at maximum expansion. The inset in panel (*c*) sketches the definition of jet width and volume, similar to Jayaprakash *et al.* (2012).
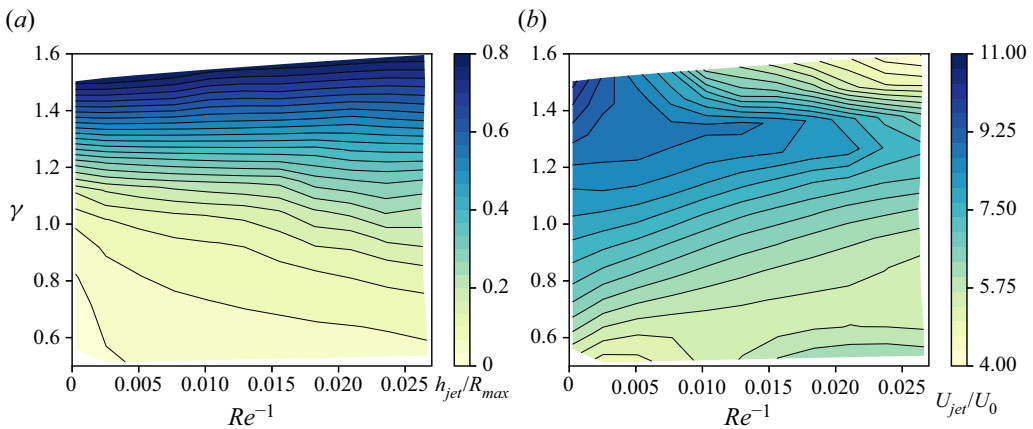

Figure 7. The distribution of normalized gap thickness h_{jet}/R_{max} and jet velocity U_{jet}/U_0 on $(1/Re, \gamma)$.

The normalized jet width R_{jet}/R_{max} for both γ values fluctuates around 0.3. Yet in a low viscous liquid, a smaller γ has a wider jet width, and this trend and the magnitude agree with the findings reported by Jayaprakash *et al.* (2012). The normalized jet volume shown in figure 6(*d*) decreases with $1/Re$. The reason is that in the more viscous liquid, the jet formation slows down so the bubble has collapsed into a smaller size when the impact occurs. The local minimum at low $1/Re$ for $\gamma = 1.1$ (the second and third markers) is the result of the particular shape of the bubble shown in figure 5.

In figure 7, we summarize the values of h_{jet} in (*a*) and U_{jet} in (*b*), which are the main factors on the formation of the wall shear stress and used for further analysis in § 6 below. At low γ, h_{jet} increases with $1/Re$ while is almost constant at high γ. Overall, the jet velocity U_{jet} decreases with viscosity and increases with γ, so h_{jet} and U_{jet} are both a complex function of these two parameters. The results for a low-viscosity liquid are consistent with experiments (Philipp & Lauterborn 1998) and simulations (Lechner *et al.* 2020).

The result here also alerted us to the use of an inviscid model for $\gamma < 1$ in the low $1/Re$ regime. Although the viscous damping plays a minor role in the low $1/Re$

regime, the formation of a thin film separating the bubble and the wall strongly relies on the appearance of liquid viscosity through forming a boundary layer. This is particular obvious in the nonlinear change of the film thickness as a function of γ for $\gamma < 1.0$ (see figure 2*b*). Yet owing to the absence of viscosity, inviscid models inherently fail to acquire stable solutions on resolving the thin film dynamics for $\gamma < 1.0$. In practice, numerical procedures may be introduced to assure a finite separation distance (Gonzalez-Avila *et al.* 2011) or to enforce a contact between the bubble and the solid boundary (Wang *et al.* 2015). Although the stability issue is overcome, these treatments prevent a modelling of the spreading flow dynamics at the solid wall. Once $\gamma > 1.0$, the film thickness increases linearly demonstrating the viscosity is unimportant for the film formation and an inviscid model is appropriate.

5. Spatio-temporal wall shear stress

We now discuss the spatio-temporal wall shear stress formation arising from an expanding and contracting bubble with the influence of the stand-off distance and liquid viscosity. The stress τ on the no-slip wall is defined and approximated as

$$\boldsymbol{\tau} = \mu \left. \frac{\mathrm{d}\boldsymbol{u_r}}{\mathrm{d}y} \right|_{y=0} \approx \mu \left. \frac{\boldsymbol{u_r}(y)}{y} \right|_{y \leq \epsilon}, \tag{5.1}$$

where $\boldsymbol{u_r}$ is the velocity of the wall-parallel flow, y is the vertical distance from the boundary and ϵ the height at which the rate of shear is constant (Schlichting & Gersten 2016). Here we use $\epsilon = 0.1\ \mu$m, which is sufficient to stay within the linearly increasing velocity regime of the boundary layer (Zeng *et al.* 2018*a*; Gonzalez-Avila *et al.* 2020).

Figures 8(*a*) and 10(*a*)–12(*a*) depict examples of spatio-temporal maps of $\tau(t, r)$ of four bubbles for two selected γ values and two viscosities. To cover the large range of the wall shear stress, its magnitude is plotted as a logarithm to the base 10. The colour of τ indicates the direction of the wall shear stress; a stress directed away from the axis of symmetry, $r = 0$, is presented in red colour and a stress towards $r = 0$ with a blue colour. The white colour reveals the stagnation regions that are annular rings. The colour bar is kept the same for all four cases for comparison. The overlaid solid line in the spatio-temporal map of each figure shows the evolution of the equivalent bubble radius until first collapse. To further illustrate the connection between the stress and the bubble dynamics, we additionally plot the bubble shape and stress distribution for four different times below the spatio-temporal map in each figure.

Let us first look at the result of the bubble in water for $\gamma = 0.7$ in figure 8. The expanding bubble creates an outward stress over the full domain and ends just shortly before reaching the maximum volume. During this stage, the stress has a maximum value of approximately 1 kPa occurring at a distance $r \approx 0.2$ mm. Inward stress appears at large distance $r > R_{max}$ at approximately $t = 31\ \mu$s and travels towards the bubble. Yet the direction of the shear stress remains outward for some regions below the bubble $R(t)$. These two regions of opposite shear stress are separated by a stagnation ring that shrinks with time. As the bubble collapses, this ring travels slowly inwards. Here the ring remains even after jet impact ($t = 86\ \mu$s) owing to a thin liquid film formed between the flattened bubble and the rigid boundary, which makes the liquid inside the film trapped and is hardly pushed by the inward flow. Before the jet impacts, the outward stresses decrease while the inward ones increase with time. Right after the jet impact, a fast jump of the outward stress is evidenced that is caused by the fast-spreading flow (see panels (*a*) and (*d*) $t = 85.5\ \mu$s).
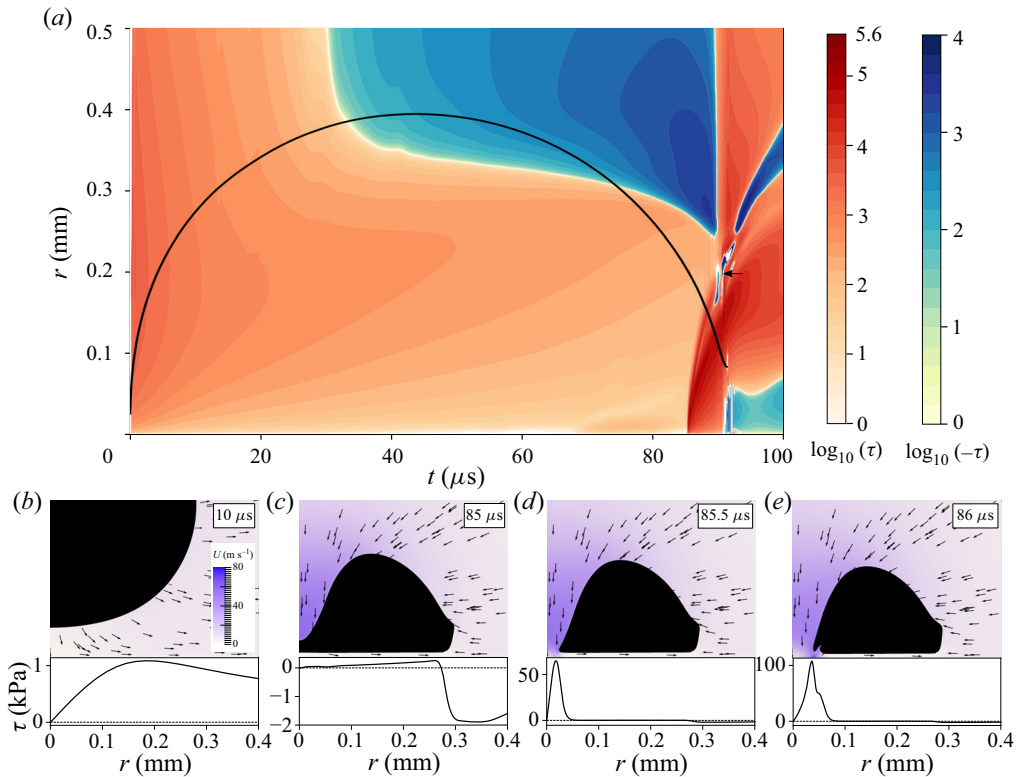
Figure 8. Spatio-temporal wall shear stress and representative flow details for bubbles of $\gamma = 0.7$ and $\mu = 10^{-3}$ Pa · s. (*a*) Wall shear stress distribution. Red and blue colours represent the outward and inward stress, respectively. Black solid line indicates the bubble equivalent radius versus time. (*b*)–(*e*) The bubble shape and flow details for different times: (*b*) expansion; (*c*) during the jet formation; (*d*) upon jet impact; (*e*) jet spreading. Bubbles are shown in black. The flow velocity is coded in blue while its direction is indicated by the arrows. The bottom of the flow frame is the solid boundary, where the wall shear stress along the radial direction r is plotted below. In the plot, dotted line indicates $\tau = 0$.

This high stress originates close to the stagnation point, $r = 0$, and travels outwards with the spreading flow.

Shock-waves developed at various stages, such as the initial expansion, jet impact and the bubble collapse, also accelerate the flow and suddenly increase the wall shear stress. Peaks of the stress appear alongside the shock-waves travelling at the speed of sound $c = 1500$ m s^{-1}. This is evidenced in figure 9. Figure 9(*a*) shows the spatio-temporal shear stress during the early expansion $0 < t < 0.5$ μs. Shortly after the bubble nucleation ($t = 0$), high outward stresses appear and decay rapidly for all distances r as the expanding shock-wave passes. Positions of those peaks follow the trajectory of the shock-wave on the solid boundary thus propagate at a velocity of $c = 1500$ m s^{-1}. Figure 9(*b*) also shows the zoomed region of figure 8 for the collapse at $91.3 < t < 91.8$ μs. Here, the shock-wave generated by the collapse of the bubble at $t = 91.4$ μs starts at a distance $r \approx 0.21$ mm, thus it accelerates the flow outwards for $r > 0.21$ mm and inwards for $r < 0.21$ mm. As a result, maxima of the outward stresses are seen for $r > 0.21$ mm and of inward stresses for $r < 0.21$ mm. Note that the wall shear stresses induced by the shock-wave are short-lived, i.e. the flow recovers within $t \approx 50$ ns.
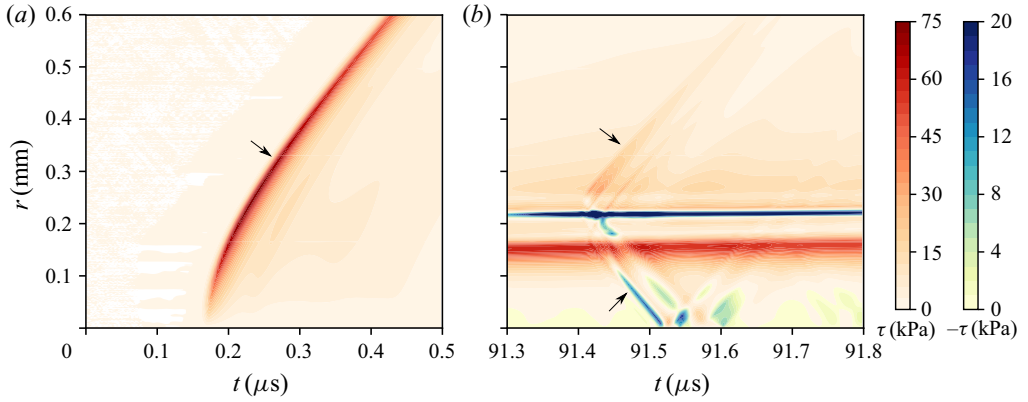
Figure 9. Zoom-in details of figure 8 during (*a*) the early expansion $0 < t < 0.5\ \mu$s and (*b*) collapse $91.3 < t < 91.8\ \mu$s. Arrows indicate the peaks of stress owing to shock-waves. Note that the colour bars have a linear scale of the wall shear stress.
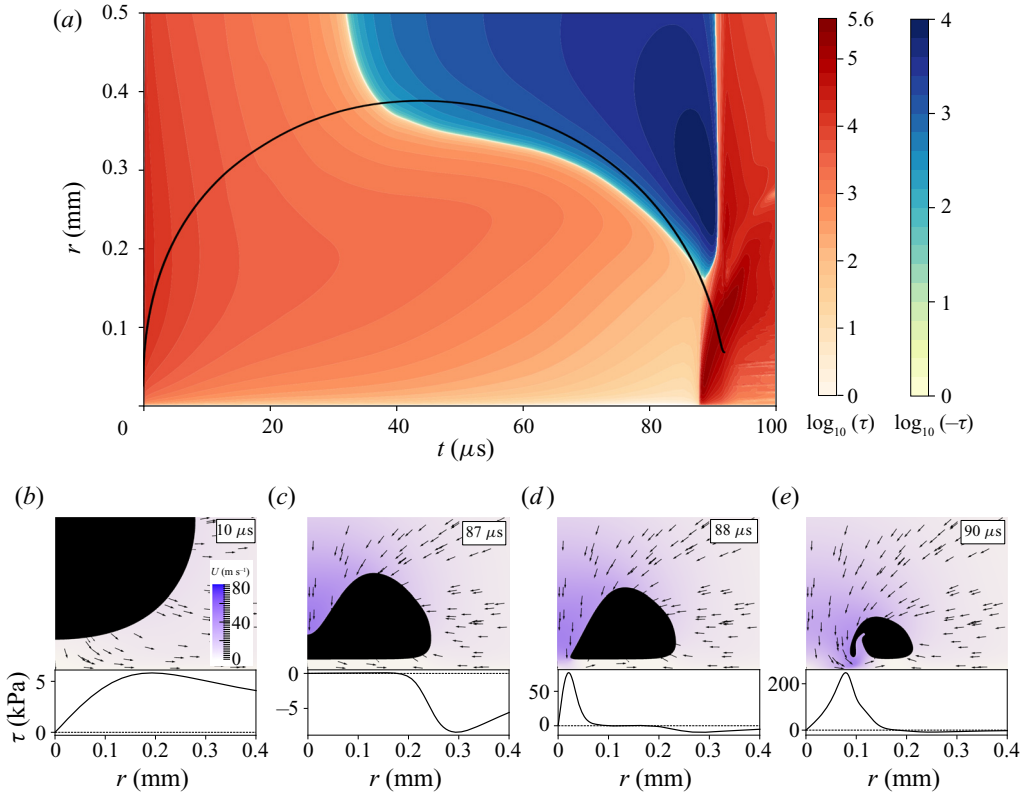

Figure 10. Spatio-temporal wall shear stress and representative flow details for bubbles of $\gamma = 0.7$ and $\mu = 0.02\ \text{Pa} \cdot \text{s}$. (*a*) Wall shear stress distribution. (*b*)–(*e*) Flow details for different times: (*b*) expansion; (*c*) during the jet formation; (*d*) upon jet impact; (*e*) jet spreading.

A similar wall shear stress pattern to figure 8 is seen in figure 10 for a bubble in liquid with higher viscosity $\mu = 0.02\ \text{Pa} \cdot \text{s}$. The stagnation ring separating inward and outward stresses is also seen owing to the same mechanism as figure 8 and remains until the jet impact. Yet the ring moves closer to the axis $r = 0$ compared with that in figure 8, which
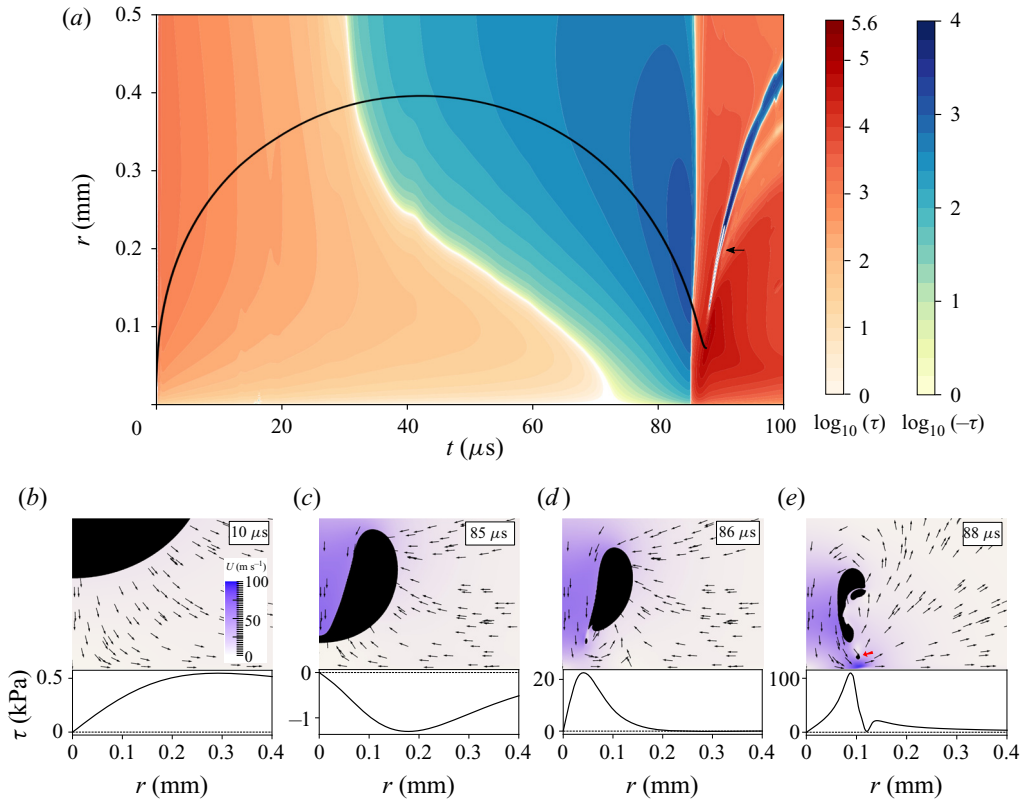
932 A14-12

Figure 11. Spatio-temporal wall shear stress and representative flow details for bubbles of $\gamma = 1.1$ and $\mu = 10^{-3}$ Pa $\cdot$ s. (*a*) Wall shear stress distribution. (*b*)–(*e*) Flow details for different times: (*b*) expansion; (*c*) during the jet formation; (*d*) upon jet impact; (*e*) jet spreading.

is the result of a thicker liquid gap. Although the flow is slowed down by higher liquid viscosity, the magnitude of the stress increases significantly for the whole time-space domain.

Figure 11 present the result of a bubble in water but with a higher stand-off distance $\gamma = 1.1$. Here, the liquid gap is much larger that allows an inward flow to develop. As a result, the stagnation ring shrinks quicker during the bubble shrinkage and reaches the axis $r = 0$ at $t = 70 \ \mu$s. Compared with figure 8, here, the outward stress during expansion and inward stress have lower magnitudes. The reason is that before jet impact, the bubble acts as a source generating a radial outflow during expansion and an inflow during contraction, and the source has a weaker effect as it moves further from the solid wall. After jet impact, the stress in the whole shown domain becomes outward within 1 μs (see panel (*d*)$t = 86 \ \mu$s), while it takes approximately 5 μs for the outward stress to develop at large r in figure 8.

With the same high stand-off distance $\gamma = 1.1$, the bubble generates a similar spatio-temporal map of wall shear stress but with higher stress magnitudes in a more viscous liquid, as shown in figure 12.

For liquids with low viscosities (figures 8 and 11), a region of local inward shear (indicated with arrows) is observed just ahead of the maximum stress, which is the result of a reversed flow generated by a high adverse pressure gradient arising from the
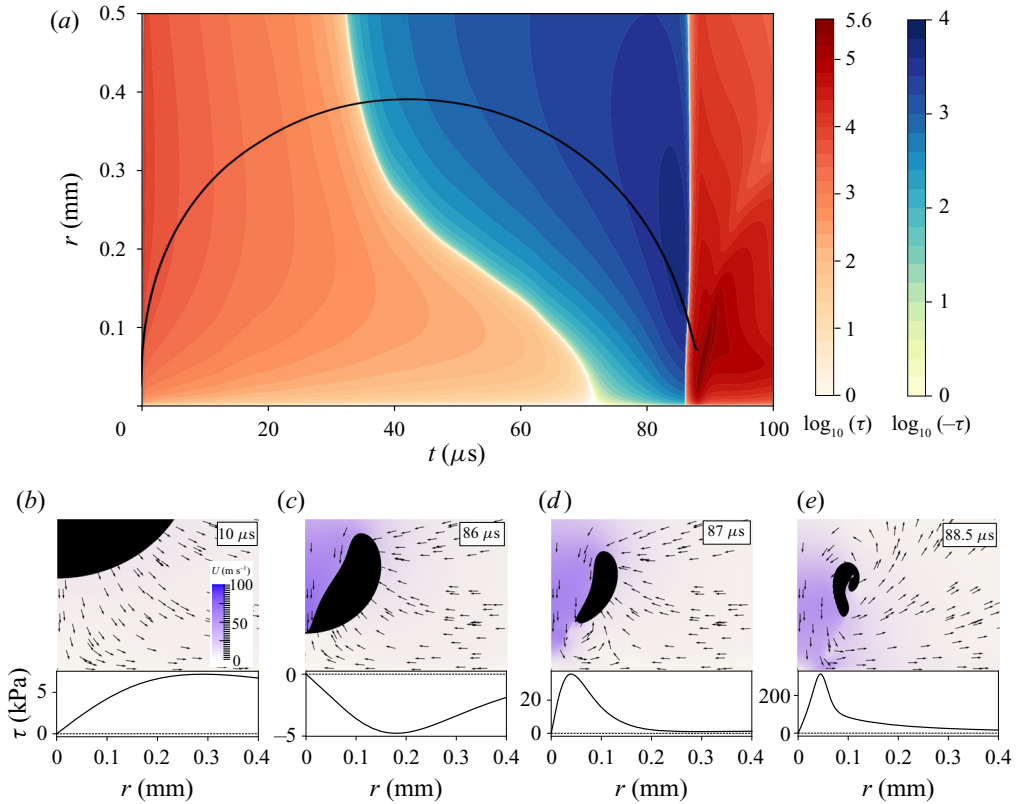
Figure 12. Spatio-temporal wall shear stress and representative flow details for bubbles of $\gamma = 1.1$ and $\mu = 0.02$ Pa · s. (*a*) Wall shear stress distribution. (*b*)–(*e*) Flow details for different times: (*b*) expansion; (*c*) during the jet formation; (*d*) upon jet impact; (*e*) jet spreading.

fast-spreading jet (Zeng *et al.* 2018*a*). However, this boundary layer separation is strongly reduced and even vanishes (figures 10 and 12) at a higher viscosity.

As seen from figures 8–12, increasing the liquid viscosity significantly increases the magnitude of both outward and inward stresses. We can further have a look at the maximum shear stress during the bubble shrinkage and jet spreading for comparison. For the cases presented, the maximum inward stresses are 2.8 kPa and 1.3 kPa in water (figures 8 and 11) while they grow to 9.9 kPa, and 5.1 kPa in a 20 times more viscous liquid (figures 10 and 12). The maximum outward stresses also increase from 110 kPa and 109 kPa to 249 kPa and 365 kPa, respectively. Although in (5.1), τ is defined proportional to the liquid viscosity μ, here, the increment of stress is nonlinear with μ, as the liquid viscosity also significantly influences the bubble dynamics and therefore the boundary flow, as shown in § 4.

6. Maximum stress distribution

We now study in figure 13 the maximum inward and outward shear stresses (τ_{mn} and τ_{mp}, respectively) over a parameter space consisting of γ and the inverse Reynolds number $1/Re$.

More specifically, τ_{mn} arises from the suction flow of the shrinking bubble, while τ_{mp} is the result of the radially spreading jet. The energy input, i.e. the initial size and
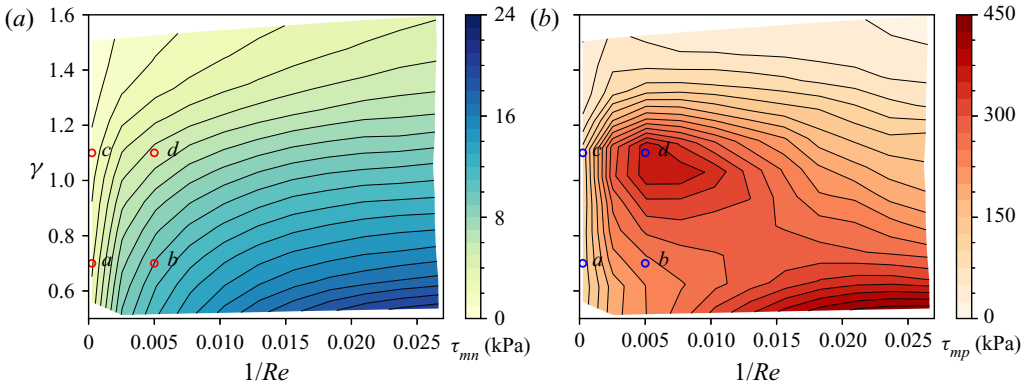
Figure 13. The maximum stress distribution on a parameter map of $(1/Re, \gamma)$, (*a*) inward and (*b*) outward. The spacing in the contour lines are 1 kPa in panel (*a*) and 25 kPa in panel (*b*). The open circles named from *a* to *d* mark the four cases in figures 8 to 12, respectively.

pressure of the bubble nucleus, is held constant at $R(t = 0) = 25$ μm and $p(r \leq R(t = 0)) = 2700$ bar. The effect of the viscosity on the maximum bubble radius R_{max} is rather mild, thus the range of $0.00025 \leq 1/Re \leq 0.027$ covers approximately the viscosity range 10^{-3} Pa · s $\leq \mu \leq 0.1$ Pa · s.

6.1. *Inward shear stress*

Let us first look at τ_{mn} in figure 13(*a*). In general, the inward stress, τ_{mn}, increases with $1/Re$ while decreases with γ monotonically. Here, τ_{mn} increases faster with $1/Re$ at low γ values as compared with higher γ values. To understand this dependency of τ_{mn}, we now apply the typical boundary layer analysis (Schlichting & Gersten 2016) to the flow profile of the expanding and collapsing bubble. At any time of the flow, we can estimate the wall shear stress as $\tau \sim \mu U_{\infty}/\delta$ with the outer radial velocity U_{∞} of the boundary layer and the boundary layer thickness δ. Within the boundary layer, the inertia forces balance the friction in the boundary layer, thus in an axisymmetric flow, we can relate

$$\rho u \partial u/\partial r \sim \mu \partial^2 u/\partial y^2. \tag{6.1}$$

The wall-perpendicular velocity gradient $\partial u/\partial y$ is of order U_{∞}/δ, thus relation (6.1) becomes

$$\rho U_{\infty} \partial U_{\infty}/\partial r \sim \mu U_{\infty}/\delta^2, \tag{6.2}$$

and the thickness of the boundary layer scales as

$$\delta \sim \left(\frac{\mu}{\rho} \frac{1}{\partial U_{\infty}/\partial r} \right)^{0.5}. \tag{6.3}$$

Then the wall shear stress can be estimated as

$$\tau \sim (\rho\mu)^{0.5} U_{\infty} (\partial U_{\infty}/\partial r)^{0.5}. \tag{6.4}$$

For the inward flow, U_{∞} decreases with r outside the bubble, therefore the expression $U_{\infty}(\partial U_{\infty}/\partial r)^{0.5}$ increases with U_{∞}. Consequently, for each bubble, the maximum inward stress τ_{mn} occurs at the maximum velocity $U_{\infty,mn}$ of the inward flow.
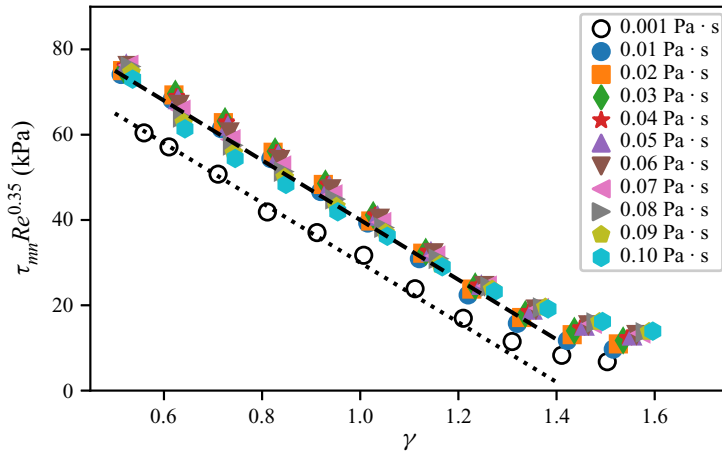
Figure 14. Graph of $\tau_{mn}Re^{0.35}$ versus γ. The dashed line represents $-70\gamma + 110$ (kPa). The doted line is $-70\gamma + 100$ (kPa). The symbols indicate liquid with various viscosity.

To estimate the scaling of the maximum inward wall shear stress with γ and $1/Re$, it seems that a knowledge of the maximum of the expression $U_{\infty,mn}(\partial U_{\infty,mn}/\partial r)$ would be necessary. Unfortunately, this expression is difficult to obtain or even estimate. Let us explain why. The magnitude of the inward stress increases during the shrinkage of the bubble. Although the rate of the change of τ is not strongly dependent on γ, the instant of time when the increase of the inwards stress ends is determined by γ. For large stand-off distance, we find that once the jet impacts on the boundary, the flow direction of the liquid near the boundary is abruptly changed from inward to outward, see figures 11(d) and 12(d). As a result, for large γ values, the maximum inward shear stress occurs just at the time of jet impact. For a bubble closer to the boundary (small γ), the liquid underneath the bubble is trapped. The jet impact results in an upwards splash into the bubble and thus prevents the jet from abruptly stopping the inward flow. Hence, the boundary layer for large $r > R(t)$ continues accelerating inwards until the bubble has further collapsed and the vortex ring, which is a result of the upwards lifted jet, spreads out, see figures 8(d,e) and 10(d,e). As a result, the inward shear stress can increase to larger values as it is affected only later by the spreading jet.

Therefore, the maximum velocity $U_{\infty,mn}$ of the inward flow is increasing with decreasing γ. Let us include the effect of the viscosity by suggesting that $\tau_{mn} \sim f(\mu^{0.5}, \gamma) \sim f((1/Re)^{0.5}, \gamma)$. We find that we can collapse the τ_{mn} values onto a line once we plot $\tau_{mn}Re^{0.35}$ versus γ rather than $\tau_{mn}Re^{0.5}$, see figure 14. The expected scaling $\tau_{mn} \sim (1/Re)^{0.5}$ reduces to $\tau_{mn} \sim (1/Re)^{0.35}$ mainly owing to the viscous dissipation of the flow for 0.001 Pa $\cdot$ s $\leq \mu \leq 0.1$ Pa $\cdot$ s. The line fitted to the range $0.5 < \gamma < 1.4$ is $\tau_{mn}Re^{0.35} = -70\gamma + 110$(kPa) for 0.01 Pa $\cdot$ s $\leq \mu \leq 0.1$ Pa $\cdot$ s, while it reduces to $\tau_{mn}Re^{0.35} = -70\gamma + 100$(kPa) for $\mu = 10^{-3}$ Pa $\cdot$ s mainly owing to a faster bubble motion that reduces the growth time of the shrinking flow in water.

6.2. *Outward shear stress*

The distribution of τ_{mp} reveals a more complex parameter space of $(1/Re, \gamma)$, see figure 13(b). At low $1/Re$, τ_{mp} first increases then decreases with γ; while at high $1/Re$, τ_{mp} always decreases with γ. The two local maxima are located at $(1/Re \approx 0.006$,

$\gamma \approx 1.0$) and ($1/Re \approx 0.026$, $\gamma \approx 0.5$), and the contour levels reveal that the gradient of the wall shear stress is stronger near the peak at low $1/Re$.

Now we focus on the location where the maximum outward shear occurs and connect its value with the bubble dynamics. Let us take τ_{mp} occurring at time $t = t_{mp}$ and a distance $r = r_{mp}$. Now at $r = r_{mp}$, the maximum radial velocity along the y direction is considered as the outer velocity of the boundary layer $U_{\infty,mp}$. Next we will use $U_{\infty,mp}$ as an intermediate variable to connect τ_{mp} with U_{jet}, h_{jet} and the liquid viscosity μ. For a further step, we can rewrite (6.3) for the boundary layer thickness as

$$\delta_{mp} \sim \left(\frac{\mu}{\rho} \frac{1}{\partial U_{\infty/,mp} \partial r} \right)^{0.5} = \mu^{0.5} \rho^{-0.5} U_{\infty,mp}^{-0.5} l_m^{0.5}, \tag{6.5}$$

where $l_m = U_{\infty,mp} / \partial U_{\infty,mp} / \partial r$ is a characteristic length for the spreading flow growing from zero to the outer velocity, which is a non-trivial function that is dependent on the bubble shape.

While tempting, the analytic similarity solution $\tau \sim r^{-11/4}$ for the steady Glauert jet (Glauert 1956) is not applicable to estimate the maximum wall shear stress of the present transient and finite-sized jets. Yet it predicts, even for a steady jet, a rapid decrease of the wall shear stress with distance r. If we neglect the bubble deformation after jet impact, a reasonable estimate of the location where the maximum outward stress occurs is at the edge of the impinging jet $r = R_{jet}$ (see figures 8–12d). This radius $R_{jet} \propto R_{max}$ increases linearly with maximum radius of the bubble (see figure 6(c), where $R_{jet}/R_{max} \approx 0.3$). Assuming conservation of mass for the incompressible impinging jet, we have $\rho U_{jet} R_{jet}^2 = \rho U_{\infty,mp} 2 R_{jet} h_{jet}$ at $r = R_{jet}$, thus $U_{\infty,mp}/U_{jet} \sim R_{max}/h_{jet}$. However, this expression is incomplete as the bubble deformation is involved and viscosity contributes through energy dissipation in the unsteady boundary layer. Therefore we use two exponents α and β that account for the geometric and viscous effects with

$$\frac{U_{\infty,mp}}{U_{jet}} \sim \left(\frac{R_{max}}{h_{jet}} \right)^{\alpha} Re^{\beta}. \tag{6.6}$$

Next we determine the values of α and β based on our computed results. Figure 15 plots the various combinations of Re and $U_{\infty,mp}/U_{jet}$ as a function of R_{max}/h_{jet} in a log–log plot. Note that the opacity of the plotted data indicates the γ value from low to high with light to dark. Figure 15 shows that the values of α and β are not constant but vary with γ. The shape reveals, as expected, two regimes with different scaling, namely for small and large γ. By fitting lines to the data in figure 15 , we obtain $(\alpha, \beta) = (0.2, 0.2)$ for $\gamma \leq 1.1$ and $(\alpha, \beta) = (1.0, 0.5)$ for $\gamma \geq 1.1$. Combining (6.5) and (6.6) into $\tau_{s,mp} \sim \mu U_{\infty,mp}/\delta_{mp}$, we obtain

$$\tau_{s,mp} \sim \mu^{0.2} h_{jet}^{-0.3} U_{jet}^{1.5} l_m^{-0.5}, \tag{6.7}$$

for $\gamma \leq 1.1$, and

$$\tau_{s,mp} \sim \mu^{-0.25} h_{jet}^{-1.5} U_{jet}^{1.5} l_m^{-0.5}, \tag{6.8}$$

for $\gamma \geq 1.1$, where $\tau_{s,mp}$ denotes the maximum outward stress from the above scaling law. The above laws can be written in a dimensionless form:

$$\bar{\tau}_{s,mp} \sim Re^{-0.2} \bar{h}_{jet}^{-0.3} \bar{U}_{jet}^{1.5} \bar{l}_m^{-0.5}, \tag{6.9}$$
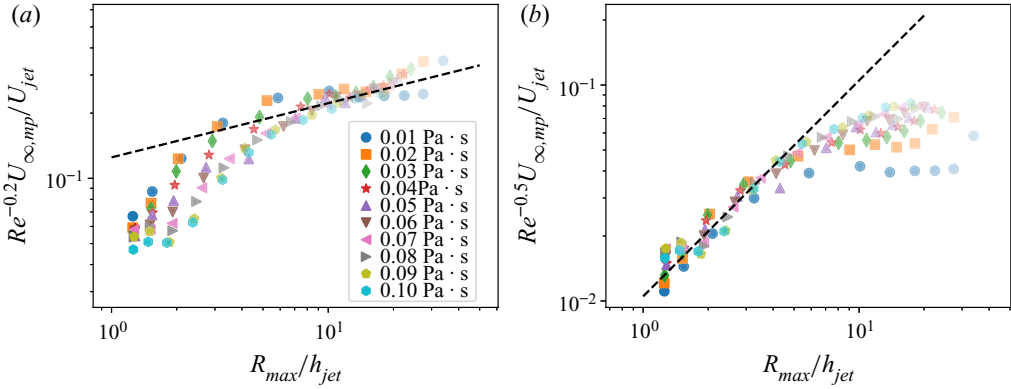
932 A14-17

Figure 15. The log–log plot for (6.6). The slopes of dashed lines are 0.2 in panel (*a*) and 1.0 in panel (*b*). The γ values from 0.5 to 1.6 for each viscosity are indicated by the opacity of the symbols from light to dark. Note the y-axis variables are different in the two plots: (*a*) data of small γ (light opacity) collapse with a slope of 0.2; (*b*) data of large γ (dark opacity) collapse with a slope of 1.0.
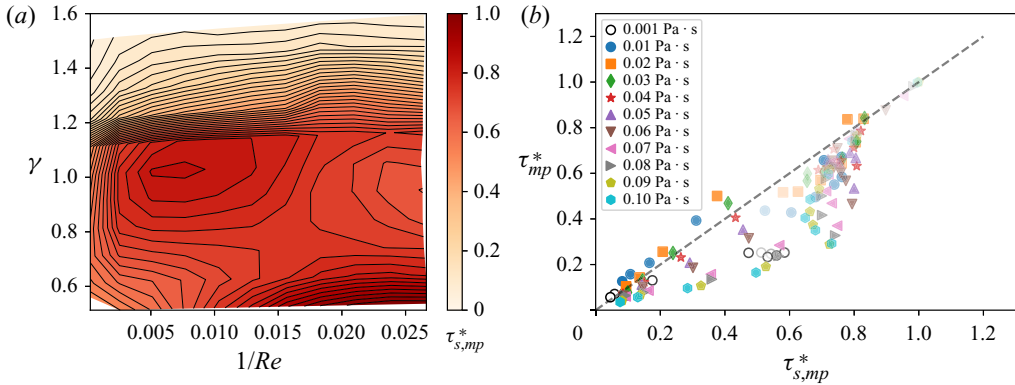

Figure 16. (*a*) Distribution of $\tau_{s,mp}^*$ on $(1/Re, \gamma)$, where $\tau_{s,mp}^*$ is the wall shear stress calculated by (6.9) and (6.10) with the input of $\bar{h}_{jet}$ and $\bar{U}_{jet}$ from figure 7 and normalized by its maximum value. (*b*) Comparison of the result using the scaling laws and the simulation result τ_{mp}^*, which is a normalized value of τ_{mp} by its maximum value. The dashed line represents $\tau^* = \tau_{mp}^*$.

for $\gamma \leq 1.1$, and

$$\bar{\tau}_{s,mp} \sim Re^{0.25}\bar{h}_{jet}^{-1.5}\bar{U}_{jet}^{1.5}\bar{l}_m^{-0.5}, \tag{6.10}$$

for $\gamma \geq 1.1$, where $\bar{\tau}_{s,mp} = \tau_{s,mp}/P_\infty$, $\bar{h}_{jet} = h_{jet}/R_{max}$, $\bar{U}_{jet} = U_{jet}/U_0$ and $\bar{l}_m = l_m/R_{max}$.

To examine the scaling, we need information of the gap thickness $\bar{h}_{jet}$ and the jet velocity $\bar{U}_{jet}$ while considering $\bar{l}_m$ has a small effect. The results are reported in § 4 figure 7. Next we insert in the relations (6.9) and (6.10) the $\bar{h}_{jet}$ and $\bar{U}_{jet}$ from the simulations shown in figure 7*a*,*b* to obtain $\bar{\tau}_{s,mp}$. How does this value compare with τ_{mp}? Figure 16(*a*) combines both $\bar{\tau}_{s,mp}$ from relations (6.7) and (6.8) in one plot; note that the plotted variable $\tau_{s,mp}^*$ is the result of $\bar{\tau}_{s,mp}$ normalized by its maximum value.

The landscape of $\tau_{s,mp}^*(1/Re, \gamma)$ shares similar features as $\tau_{mp}(1/Re, \gamma)$ in figure 13(*b*) with both local maximum values occurring at almost the same locations. For comparison, we plot $\tau_{s,mp}^*$ against the normalized τ_{mp}, τ_{mp}^*, in figure 16(*b*) and we find, overall, a

932 A14-18

linear relationship. Yet there are deviations that are caused by the richness of the flow field and resulting bubble shapes briefly before the bubble collapse. For example, we observe a splitting of the main bubble resulting in daughter toroidal bubbles close to the boundary for $\gamma > 1.0$ (see small red arrow in figure 11*e*). It is expected that these flows alter notably the wall shear stress by affecting the characteristic length l_m in (6.7) and (6.8). These complex shapes are relevant and seen in experiments, e.g. by Brujan *et al.* (2002), Zhang *et al.* (2015). Overall, the scaling of relations (6.9) and (6.10) capture the dependence of the maximum stress as a function of viscosity, μ, gap thickness, h_{jet}, and jet velocity, U_{jet}.

7. Conclusion

In summary, we have conducted a parameter study of the wall shear stress induced by jetting cavitation bubbles with a focus on the effect of liquid viscosity and bubble stand-off distance. The gap formed between the bubble's lower interface and wall influences the formation of both the inward and the outward stress patterns, which leads to complex spatio-temporal distributions varying with μ and γ. We provide scaling laws for the maximum inward and outward stresses. The maximum inward stress induced by the shrinking bubble can be predicted with $\tau_{mn}Re^{0.35} = -70\gamma + 110$ (kPa) for $0.5 < \gamma < 1.4$. The scaling of the maximum outward stress varies with γ. For $0.5 \le \gamma \le 1.1$, $\tau_{mp} \sim \mu^{0.2}h_{jet}^{-0.3}U_{jet}^{1.5}$, while it changes to $\tau_{mp} \sim \mu^{-0.25}h_{jet}^{-1.5}U_{jet}^{1.5}$ for $1.1 \le \gamma \le 1.6$. These results indicate that the stress decreases rapidly with the gap thickness especially when $\gamma \ge 1.1$. Surface cleaning from the first inertial cavitation bubble collapse may be optimum for $\gamma \le 1.1$ and has been suggested by Reuter & Mettin (2016).

The stress from the second expansion and subsequent bubble oscillation has peak values of a few kPa, which are considerably smaller than those during the first oscillation cycle. The reason is that a large fraction of the potential bubble energy is lost during the first collapse (Vogel, Lauterborn & Timm 1989; Zeng *et al.* 2018*a*). Yet the present analysis does not account for bubbles translating along the boundary and oscillate for many oscillations. These more realistic studies demand for a more complete model with energy loss arising from collapse as a function of γ and μ as well as accounting for the then 3-dimensional problem. Interestingly, the present simulations predict a stronger wall shear stress for inward flow with increasing viscosity; while for outward flow, local maximum wall shear stress is seen as viscosity increases. As this finding is robust for all stand-off distances, we suggest to explore liquids with approximately 20 times higher viscosity than water. We expect that these may provide an enhanced cleaning as compared to low-viscosity solvents such as aqueous detergent solutions or hydrofluoroethers commonly used as cleaning solutions.

Author ORCIDs.

ⓘ Qingyun Zeng https://orcid.org/0000-0003-1369-8236;

ⓘ Claus-Dieter Ohl https://orcid.org/0000-0001-5333-4723.

References

BEIG, S.A., ABOULHASANZADEH, B. & JOHNSEN, E. 2018 Temperatures produced by inertially collapsing bubbles near rigid surfaces. *J. Fluid Mech.* **852**, 105–125.

BLAKE, J.R. & GIBSON, D.C. 1987 Cavitation bubbles near boundaries. *Annu. Rev. Fluid Mech.* **19** (1), 99–123.

BRACKBILL, J.U., KOTHE, D.B. & ZEMACH, C. 1992 A continuum method for modeling surface tension. *J. Comput. Phys.* **100** (2), 335–354.

BRENNEN, C.E. 2014 *Cavitation and Bubble Dynamics*. Cambridge University Press.

BRUJAN, E.A., KEEN, G.S., VOGEL, A. & BLAKE, J.R. 2002 The final stage of the collapse of a cavitation bubble close to a rigid boundary. *Phys. Fluids* **14** (1), 85–92.

CHAHINE, G.L., KAPAHI, A., CHOI, J.-K. & HSIAO, C.-T. 2016 Modeling of surface cleaning by cavitation bubble dynamics and collapse. *Ultrason. Sonochem.* **29**, 528–549.

DENNER, F., EVRARD, F. & VAN WACHEM, B. 2020 Modeling acoustic cavitation using a pressure-based algorithm for polytropic fluids. *Fluids* **5** (2), 69.

DIJKINK, R. & OHL, C.-D. 2008 Measurement of cavitation induced wall shear stress. *Appl. Phys. Lett.* **93** (25), 254107.

GLAUERT, M.B. 1956 The wall jet. *J. Fluid Mech.* **1** (6), 625–643.

GONZALEZ-AVILA, S.R., VAN BLOKLAND, A.C., ZENG, Q. & OHL, C.-D. 2020 Jetting and shear stress enhancement from cavitation bubbles collapsing in a narrow gap. *J. Fluid Mech.* **884**, A23.

GONZALEZ-AVILA, S.R., KLASEBOER, E., KHOO, B.C. & OHL, C.-D. 2011 Cavitation bubble dynamics in a liquid gap of variable height. *J. Fluid Mech.* **682**, 241–260.

HAN, B., KÖHLER, K., JUNGNICKEL, K., METTIN, R., LAUTERBORN, W. & VOGEL, A. 2015 Dynamics of laser-induced bubble pairs. *J. Fluid Mech.* **771**, 706–742.

JAYAPRAKASH, A., HSIAO, C.-T. & CHAHINE, G. 2012 Numerical and experimental study of the interaction of a spark-generated bubble and a vertical wall. *J. Fluids Engng* **134** (3), 031301.

JOHNSEN, E. & COLONIUS, T.I.M. 2009 Numerical simulations of non-spherical bubble collapse. *J. Fluid Mech.* **629**, 231–262.

KOCH, M., LECHNER, C., REUTER, F., KÖHLER, K., METTIN, R. & LAUTERBORN, W. 2016 Numerical modeling of laser generated cavitation bubbles with the finite volume and volume of fluid method, using openfoam. *Comput. Fluids* **126**, 71–90.

KOUKOUVINIS, P., STROTOS, G., ZENG, Q., GONZALEZ-AVILA, S.R., THEODORAKAKOS, A., GAVAISES, M. & OHL, C.-D. 2018 Parametric investigations of the induced shear stress by a laser-generated bubble. *Langmuir* **34** (22), 6428–6442.

LAUER, E., HU, X.Y., HICKEL, S. & ADAMS, N.A. 2012 Numerical modelling and investigation of symmetric and asymmetric cavitation bubble dynamics. *Comput. Fluids* **69**, 1–19.

LECHNER, C., LAUTERBORN, W., KOCH, M. & METTIN, R. 2020 Jet formation from bubbles near a solid boundary in a compressible liquid: numerical study of distance dependence. *Phys. Rev. Fluids* **5** (9), 093604.

LEE, M., KLASEBOER, E. & KHOO, B.C. 2007 On the boundary integral method for the rebounding bubble. *J. Fluid Mech.* **570**, 407–429.

LI, S., HAN, R., ZHANG, A.M. & WANG, Q.X. 2016 Analysis of pressure field generated by a collapsing bubble. *Ocean Engng* **117**, 22–38.

MILLER, S.T., JASAK, H., BOGER, D.A., PATERSON, E.G. & NEDUNGADI, A. 2013 A pressure-based, compressible, two-phase flow finite volume method for underwater explosions. *Comput. Fluids* **87**, 132–143.

OHL, C.-D., ARORA, M., DIJKINK, R., JANVE, V. & LOHSE, D. 2006*a* Surface cleaning from laser-induced cavitation bubbles. *Appl. Phys. Lett.* **89** (7), 074102.

OHL, C.-D., ARORA, M., IKINK, R., DE JONG, N., VERSLUIS, M., DELIUS, M. & LOHSE, D. 2006*b* Sonoporation from jetting cavitation bubbles. *Biophys. J.* **91** (11), 4285–4295.

PHILIPP, A. & LAUTERBORN, W. 1998 Cavitation erosion by single laser-produced bubbles. *J. Fluid Mech.* **361**, 75–116.

PLESSET, M.S. & CHAPMAN, R.B. 1971 Collapse of an initially spherical vapour cavity in the neighbourhood of a solid boundary. *J. Fluid Mech.* **47** (2), 283–290.

POPINET, S. & ZALESKI, S. 2002 Bubble collapse near a solid boundary: a numerical study of the influence of viscosity. *J. Fluid Mech.* **464**, 137–163.

RAU, K.R., QUINTO-SU, P.A., HELLMAN, A.N. & VENUGOPALAN, V. 2006 Pulsed laser microbeam-induced cell lysis: time-resolved imaging and analysis of hydrodynamic effects. *Biophys. J.* **91** (1), 317–329.

REUTER, F. & KAISER, S.A. 2019 High-speed film-thickness measurements between a collapsing cavitation bubble and a solid surface with total internal reflection shadowmetry. *Phys. Fluids* **31** (9), 097108.

REUTER, F., LAUTERBORN, S., METTIN, R. & LAUTERBORN, W. 2017 Membrane cleaning with ultrasonically driven bubbles. *Ultrason. Sonochem.* **37**, 542–560.

REUTER, F. & METTIN, R. 2016 Mechanisms of single bubble cleaning. *Ultrason. Sonochem.* **29**, 550–562.

REUTER, F. & METTIN, R. 2018 Electrochemical wall shear rate microscopy of collapsing bubbles. *Phys. Rev. Fluids* **3** (6), 063601.

RUSCHE, H. 2003 Computational fluid dynamics of dispersed two-phase flows at high phase fractions. PhD thesis, Imperial College London (University of London).

SCHLICHTING, H. & GERSTEN, K. 2016 *Boundary-Layer Theory*. Springer.

SUPPONEN, O., OBRESCHKOW, D., TINGUELY, M., KOBEL, P., DORSAZ, N. & FARHAT, M. 2016 Scaling laws for jets of single cavitation bubbles. *J. Fluid Mech.* **802**, 263–293.

TRUMMLER, T., BRYNGELSON, S.H., SCHMIDMAYER, K., SCHMIDT, S.J., COLONIUS, T. & ADAMS, N.A. 2020 Near-surface dynamics of a gas bubble collapsing above a crevice. *J. Fluid Mech.* **899**, A16.

VOGEL, A., LAUTERBORN, W. & TIMM, R. 1989 Optical and acoustic investigations of the dynamics of laser-produced cavitation bubbles near a solid boundary. *J. Fluid Mech.* **206**, 299–338.

WANG, Q. 2014 Multi-oscillations of a bubble in a compressible liquid near a rigid boundary. *J. Fluid Mech.* **745**, 509–536.

WANG, Q., LIU, W., ZHANG, A.M. & SUI, Y. 2015 Bubble dynamics in a compressible liquid in contact with a rigid boundary. *Interface Focus* **5** (5), 20150048.

WELLER, H.G., TABOR, G., JASAK, H. & FUREBY, C. 1998 A tensorial approach to computational continuum mechanics using object-oriented techniques. *Comput. Phys.* **12** (6), 620–631.

ZENG, Q., GONZALEZ-AVILA, S.R., DIJKINK, R., KOUKOUVINIS, P., GAVAISES, M. & OHL, C.-D. 2018*a* Wall shear stress from jetting cavitation bubbles. *J. Fluid Mech.* **846**, 341–355.

ZENG, Q., GONZALEZ-AVILA, S.R. & OHL, C.-D. 2020 Splitting and jetting of cavitation bubbles in thin gaps. *J. Fluid Mech.* **896**, A28.

ZENG, Q., GONZALEZ-AVILA, S.R., TEN VOORDE, S. & OHL, C.-D. 2018*b* Jetting of viscous droplets from cavitation-induced Rayleigh–Taylor instability. *J. Fluid Mech.* **846**, 916–943.

ZHANG, A.M., LI, S. & CUI, J. 2015 Study on splitting of a toroidal bubble near a rigid boundary. *Phys. Fluids* **27** (6), 062102.

ZHANG, A.M. & LIU, Y.L. 2015 Improved three-dimensional bubble dynamics model based on boundary element method. *J. Comput. Phys.* **294**, 208–223.